

Entanglement of Spin-Pair Qubits with Intrinsic Dephasing Times Exceeding a Minute

H. P. Bartling,^{1,2} M. H. Abobeih,^{1,2} B. Pingault,^{1,2,3} M. J. Degen,^{1,2} S. J. H. Loenen,^{1,2} C. E. Bradley,^{1,2} J. Randall,^{1,2} M. Markham,⁴ D. J. Twitchen,⁴ and T. H. Taminiau^{1,2,*}

¹*QuTech, Delft University of Technology, P.O. Box 5046, 2600 GA Delft, Netherlands*

²*Kavli Institute of Nanoscience Delft, Delft University of Technology, P.O. Box 5046, 2600 GA Delft, Netherlands*

³*John A. Paulson School of Engineering and Applied Sciences, Harvard University, 29 Oxford Street, Cambridge, Massachusetts 02138, USA*

⁴*Element Six, Fermi Avenue, Harwell Oxford, Didcot, Oxfordshire, OX11 0QR, United Kingdom*



(Received 15 June 2021; accepted 19 January 2022; published 14 March 2022)

Understanding and protecting the coherence of individual quantum systems is a central challenge in quantum science and technology. Over the past decades, a rich variety of methods to extend coherence have been developed. A complementary approach is to look for naturally occurring systems that are inherently protected against decoherence. Here, we show that pairs of identical nuclear spins in solids form intrinsically long-lived qubits. We study three carbon-13 pairs in diamond and realize high-fidelity measurements of their quantum states using a single nitrogen-vacancy center in their vicinity. We then reveal that the spin pairs are robust to external perturbations due to a combination of three phenomena: a decoherence-free subspace, a clock transition, and a variant on motional narrowing. The resulting inhomogeneous dephasing time is $T_2^* = 1.9(3)$ min, the longest reported for individually controlled qubits. Finally, we develop complete control and realize an entangled state between two spin pairs through projective parity measurements. These long-lived qubits are abundantly present in diamond and other solids and provide new opportunities for ancilla-enhanced quantum sensing and for robust memory qubits for quantum networks.

DOI: [10.1103/PhysRevX.12.011048](https://doi.org/10.1103/PhysRevX.12.011048)

Subject Areas: Condensed Matter Physics
Quantum Physics, Quantum Information

I. INTRODUCTION

Solid-state spins provide a versatile platform for investigating quantum physics and realizing quantum technologies [1–28]. A central challenge is to protect spin qubits from decoherence due to their environment. Various methods to extend coherence times have been developed for spin ensembles [2,7–9] as well as individually controlled spin qubits [1,3–6,10,11,16,17]. These methods include the precise tuning of magnetic fields to create magnetic-field-insensitive clock transitions [7,9,10,29,30], decoherence-free subspaces to protect against correlated noise [5,10,19,30], dynamical decoupling to mitigate slowly varying noise [2–4,8,9,11,31], real-time Hamiltonian estimation [6], quantum error correction [16,17,32], and isotopic purification to remove the spin background [2,3,8].

Here, we take a different approach: we look for naturally occurring qubits that are inherently protected against decoherence. We investigate pairs of identical interacting nuclear spins [33]. Such spin pairs are naturally and abundantly present in solids like diamond, silicon, silicon-carbide, germanium, graphene, and MoS₂ [11,13,14,21,22]. Traditionally, the dynamics of such spin pairs have been regarded as a primary noise source for solid-state spin qubits [7,11,21,22,37]. In contrast, we show that spin pairs themselves provide individually controllable and decoherence-protected quantum systems. First, we develop high-fidelity initialization and single-shot readout of multiple spin-pair qubits. Then, we investigate their coherence and show that they are inherently protected by a combination of a decoherence-free subspace, a clock transition, and a variant on motional narrowing. Finally, we highlight the potential of these spin pairs as qubits by creating an entangled state of two spin pairs through sequential nondestructive parity measurements.

*T.H.Taminiau@TUDelft.nl

Published by the American Physical Society under the terms of the [Creative Commons Attribution 4.0 International license](https://creativecommons.org/licenses/by/4.0/). Further distribution of this work must maintain attribution to the author(s) and the published article's title, journal citation, and DOI.

II. SPIN PAIRS

The system that we investigate is illustrated in Fig. 1(a). We consider three pairs of coupled ¹³C nuclear spins in the

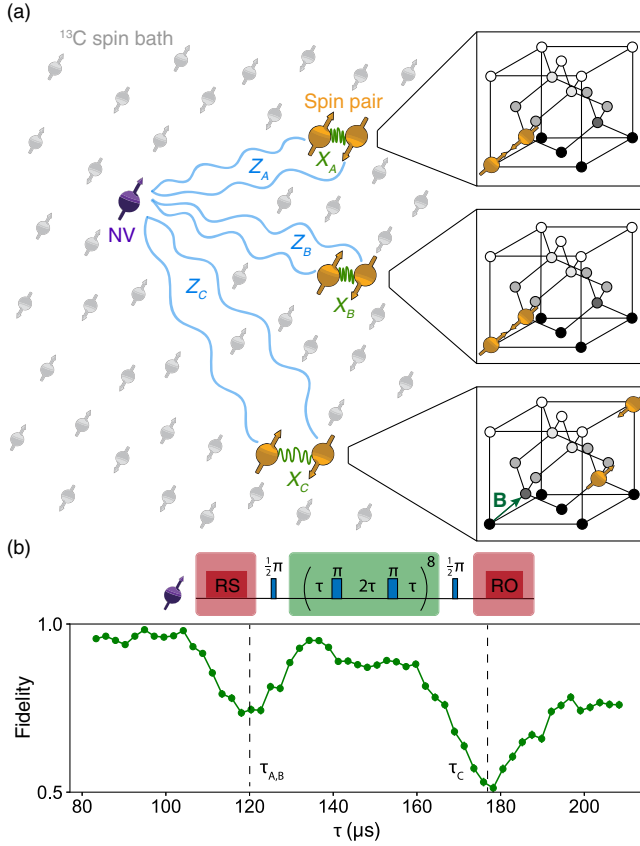


FIG. 1. System and basic spectroscopy. (a) We study three ^{13}C spin pairs (A, B, and C) in a diamond. The pairs are detected and controlled using a nearby NV center. The insets show the spatial configuration of the pairs. Pairs A and B are nearest-neighbor pairs oriented along the external magnetic field B_z . For pair C, we show one of the three possible orientations (Appendix H). The main source of decoherence is the surrounding bath of ^{13}C spins (1.1% abundance). (b) Sensing the pair pseudospins [11,13,14]. The NV electron spin is prepared in a superposition, and a periodic sequence of π pulses is applied. If the interpulse delay is resonant with the dynamics of a pair, a loss of electron coherence is observed. We set $\tau = m2\pi/\omega_L$ with m an integer and ω_L the ^{13}C Larmor frequency to avoid interactions with individual ^{13}C spins [11,14]. The vertical lines mark the values for τ used in this work for the three pairs ($\tau_A = \tau_B = 120.330 \mu\text{s}$ and $\tau_C = 177.026 \mu\text{s}$). The NV spin is prepared (RS) and read out (RO) optically (Appendix A). The error bars represent one standard deviation.

vicinity of a nitrogen-vacancy (NV) center in a diamond at 3.7 K. The NV center provides a controllable electron spin with long coherence times that can be initialized and measured optically [2,4,11,14,16–18]. Because the NV spin creates a switchable local magnetic-field gradient over each pair, it can be used to sense and manipulate the spin pairs [11,13,14], despite their excellent protection from external influences.

A spin-1/2 pair is described by four states: $|\uparrow\uparrow\rangle$, $|\uparrow\downarrow\rangle$, $|\downarrow\uparrow\rangle$, and $|\downarrow\downarrow\rangle$. We focus on the dynamics in the antiparallel

subspace and define a pseudospin spanned by $|\uparrow\rangle = |\uparrow\downarrow\rangle$ and $|\downarrow\rangle = |\downarrow\uparrow\rangle$ [11,13,14]. The pseudospin Hamiltonian is (Appendix C)

$$H = X\hat{I}_x + m_s Z\hat{I}_z, \quad (1)$$

in which \hat{I}_z and \hat{I}_x are spin-1/2 operators. X is the dipolar coupling between the ^{13}C spins, which creates the evolution $|\uparrow\rangle \leftrightarrow |\downarrow\rangle$ (flip flops). $m_s = \{-1, 0, +1\}$ is the NV spin projection, and Z is the difference between the two NV- ^{13}C hyperfine couplings (Appendix C).

Pair A and pair B are nearest-neighbor pairs oriented along the external magnetic field with $X_A = X_B = 2080.9900(3)$ Hz, $Z_A = 130(1)$ Hz, and $Z_B = 91(2)$ Hz (see measurements below). Pair C has a larger spatial separation between the spins resulting in $X_C = 188.33(2)$ Hz, and $Z_C = 2802(2)$ Hz. In the following, we develop initialization, control, and measurement for pairs A and B, for which $X \gg Z$ (see Appendix D for pair C control, for which $Z \gg X$).

Previous work demonstrates that the pseudospin of pairs can be detected through decoupling sequences that toggle the $m_s Z\hat{I}_z$ term by periodically inverting the NV electron spin [Fig. 1(b)] [11,13,14]. For an interpulse delay of $2\tau = \pi/\omega_r$, with $\omega_r = \sqrt{X^2 + (Z/2)^2}$, the sequence is resonant with the pseudospin dynamics, and the effective NV-pair interaction is of the form $\hat{S}_z\hat{I}_z$, with \hat{S}_z the spin operator for the NV electron spin [11,13,14]. The NV center thus accumulates a phase that depends on the z projection of the pseudospin. We use the NV center as a sensor to detect the spin pairs in its environment by sweeping τ [Fig. 1(b)] [11,13,14] and find the resonances for pairs A and B ($\tau = 120.330 \mu\text{s}$) and pair C ($\tau = 177.026 \mu\text{s}$).

III. INITIALIZATION AND READOUT

We start by developing projective single-shot measurements. Unlike all previous work, which is limited to manipulating mixed states of the parallel and antiparallel subspaces [11], these measurements enable us to initialize and measure the complete state of the spin pairs with high contrast.

Our method is based on repeated nondestructive measurements and illustrated in Fig. 2. Each repetition comprises an interaction period between the NV and the pair pseudospin before optical readout. During the interaction, the NV electron spin accumulates a positive (negative) phase if a pair is in $|\uparrow\rangle$ ($|\downarrow\rangle$). For a pair in the parallel subspace ($|\uparrow\uparrow\rangle$ or $|\downarrow\downarrow\rangle$), the NV spin does not accumulate any phase. We choose τ such that pairs A and B interact with the NV spin simultaneously. Therefore, the NV spin accumulates a phase that depends on which of the 16 possible states the two pairs are in [Fig. 2(c)]. By repeatedly applying this sequence, we realize a projective

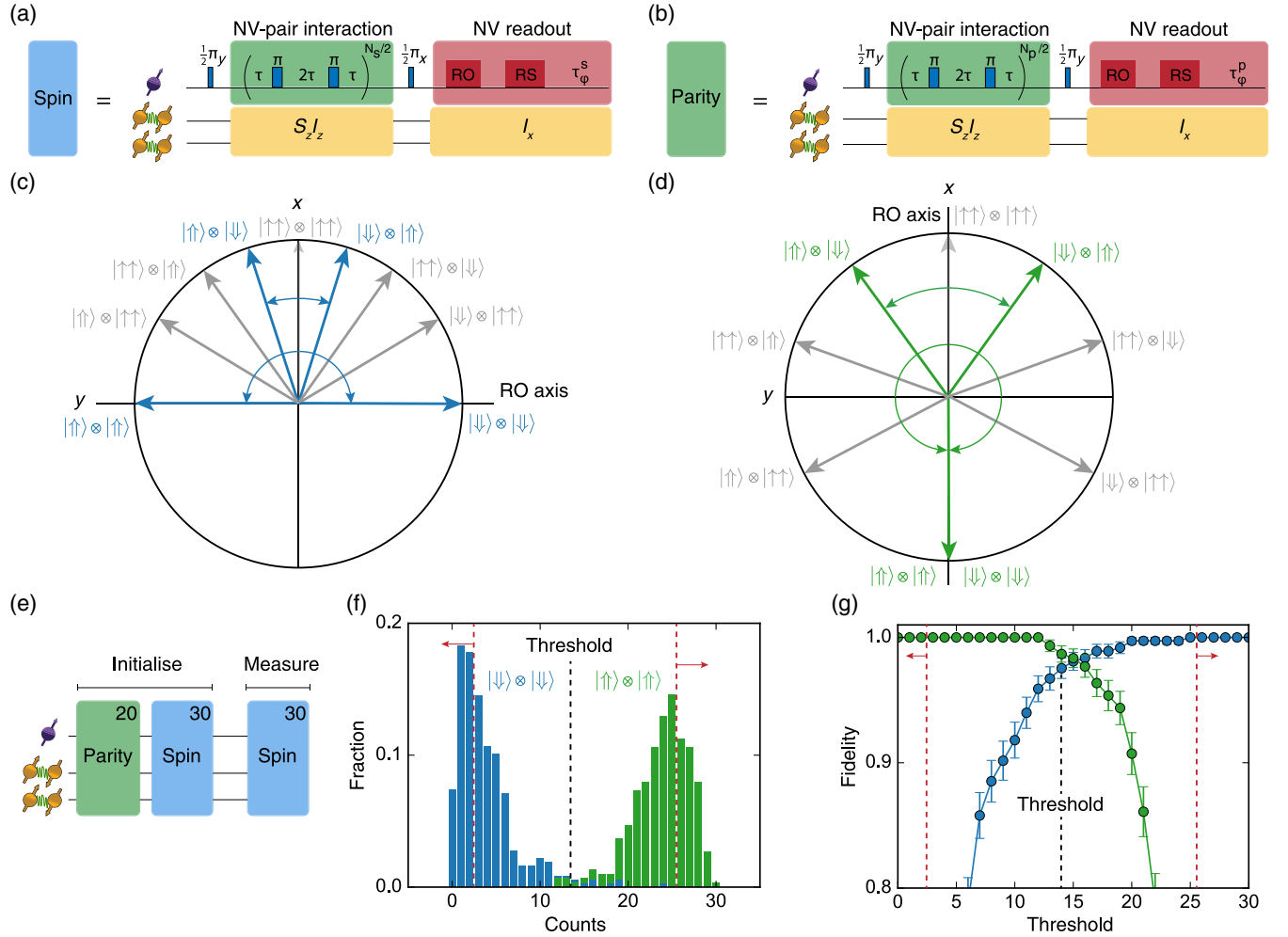


FIG. 2. Projective spin and parity measurements for pairs A and B . (a) Sequence to measure the pseudospin states. The NV electron spin starts in $m_s = 0$. The $\hat{S}_z \hat{I}_z$ interaction sequence ($\tau = 120.330 \mu\text{s}$ and $N_s = 14$) maps the state of the two pairs onto the NV spin. The NV spin is subsequently read out (RO) and reset (RS) to $m_s = 0$. We synchronize subsequent repetitions by calibrating a waiting time $\tau_\phi^s = 323.5 \mu\text{s}$ to compensate for the \hat{I}_x evolution during NV readout. This ensures that the full sequence duration is a multiple of $1/X$. (b) Sequence to measure the pseudospin parity ($N_p = 20$, Supplemental Sec. IV [38]). We set $\tau_\phi^p = 81 \mu\text{s}$ to synchronize subsequent measurements [sequence duration a multiple of $1/(2X)$]. (c) XY plane of the NV Bloch sphere showing the possible phases accumulated in the spin measurement. The NV spin starts along x and picks up a positive (negative) phase for a pair in $|\uparrow\uparrow\rangle$ ($|\downarrow\downarrow\rangle$) and no phase for a pair in a parallel state ($|\uparrow\uparrow\rangle$ or $|\downarrow\downarrow\rangle$). Reading out along the y axis distinguishes the four pseudospin states (blue). Note that $|\downarrow\downarrow\rangle$ (not shown) gives the same result as $|\uparrow\uparrow\rangle$. (d) XY plane of the NV Bloch sphere under parity readout. The initial state (x axis) and the readout axis (x axis) are identical so that the parity of pairs A and B is measured. (e) Measurement sequence to calibrate single-shot readout and initialization. The top right of each block indicates the number of repetitions. The optimal number of spin readouts is 30 (Supplemental Sec. III [38]). (f) Conditional histograms for 30 spin readouts after initialization in $|\uparrow\uparrow\rangle \otimes |\uparrow\uparrow\rangle$ (green) and $|\downarrow\downarrow\rangle \otimes |\downarrow\downarrow\rangle$ (blue). The initialization conditions for the 30 preceding spin readouts are indicated in red. (g) Combined initialization and readout fidelity for $|\uparrow\uparrow\rangle \otimes |\uparrow\uparrow\rangle$ (green) and $|\downarrow\downarrow\rangle \otimes |\downarrow\downarrow\rangle$ (blue) for 30 spin readouts. We find an optimum of $F = 98.1(5)\%$ for a decision threshold of 14 out of 30. The error bars represent one standard deviation.

measurement that can distinguish multiple states in a single shot and with high contrast.

We construct two types of measurements by setting different interaction times and NV readout axes [Figs. 2(a) and 2(b)]. The “spin” measurement distinguishes the four pseudospin states $\{|\uparrow\uparrow\rangle, |\uparrow\downarrow\rangle, |\downarrow\uparrow\rangle, \text{ and } |\downarrow\downarrow\rangle\}$; Figs. 2(a) and 2(c). The “parity” measurement distinguishes only the pseudospin parity of the two pairs $\{|\uparrow\uparrow\rangle, |\downarrow\downarrow\rangle\}$: even

parity versus $\{|\uparrow\downarrow\rangle, |\downarrow\uparrow\rangle\}$: odd parity; Figs. 2(b) and 2(d)]. Because the pseudospins evolve as $|\uparrow\uparrow\rangle \leftrightarrow |\downarrow\downarrow\rangle$ with a frequency of approximately X during the NV spin readout, each repetition must be timed to align the measurement axes. This synchronization of repeated nondestructive measurements to the system evolution is similar to the case of repeated measurements on individual spins, e.g., in the context of quantum algorithms [16,23], atomic

frequency locking and quantum Zeno dynamics [24], and weak measurement sequences [25,26].

We combine these sequences to realize high-fidelity initialisation and measurement [Fig. 2(e)]. We first apply the parity measurement sequence (20 repetitions) to herald preparation in an even parity state and to exclude the cases for which one or both pairs are in their parallel subspace. Then, we apply a spin measurement (30 repetitions) to herald either $|\uparrow\uparrow\rangle$ or $|\downarrow\downarrow\rangle$. Finally, we measure the pseudospin state with another spin measurement (30 repetitions). The resulting conditional histograms show well-isolated distributions [Fig. 2(f)], and an optimization of the measurement decision threshold [Fig. 2(g)] yields a combined initialization and readout fidelity of 98.1(5)%. We refer to Supplemental Material [38] for the full optimization procedure.

IV. COHERENCE OF PAIRS A AND B

We use the developed high-contrast measurements to investigate the coherence of pairs *A* and *B*. First, we perform a free-evolution experiment with the NV spin in $m_s = -1$ [Fig. 3(a)], for which the NV-pair coupling is on. Because the pseudospin precession frequency $\sqrt{X^2 + Z^2}$ is different for the pairs ($Z_A \neq Z_B$), this measurement reveals the presence of the two pairs and characterizes their couplings *Z* to the NV. The two frequencies observed give $Z_A = 130(1)$ Hz and $Z_B = 91(2)$ Hz (Appendix B). We obtain the dephasing times from a Fourier transform [Fig. 3(a)]: $T_{2,A}^* = 0.26(2)$ s and $T_{2,B}^* = 0.39(6)$ s (Appendix B). These values are 1–2 orders of magnitude larger than for individual ^{13}C spins in the same sample [4].

Second, we perform the same experiment with the NV spin in $m_s = 0$, so that the coupling to the NV is effectively turned off. Now both pairs precess with frequency $X_A = X_B = 2080.9900(3)$ Hz [Fig. 3(b)], and a coherent oscillation that extends past 70 s is observed. To extract the dephasing time, we measure the oscillation amplitude at various times [Fig. 3(c)]. The resulting decay yields $T_2^* = 1.9(3)$ min, a 4-orders-of-magnitude improvement over an individual spin [4] and the longest inhomogeneous dephasing time reported for any individually controllable quantum system [29].

V. DECOHERENCE MECHANISMS

We now elucidate the mechanisms which lead to these remarkable coherence properties. We add a magnetic-field noise term $\Delta Z(t)$ to the pseudospin Hamiltonian:

$$H = X\hat{I}_x + [m_s Z + \Delta Z(t)]\hat{I}_z. \quad (2)$$

The first mechanism which enhances the coherence is the decoherence-free subspace [30,39] formed by the pseudo-spin states. Because the spins are identical, $\Delta Z(t)$ is given by the fluctuations of the magnetic-field *difference* between

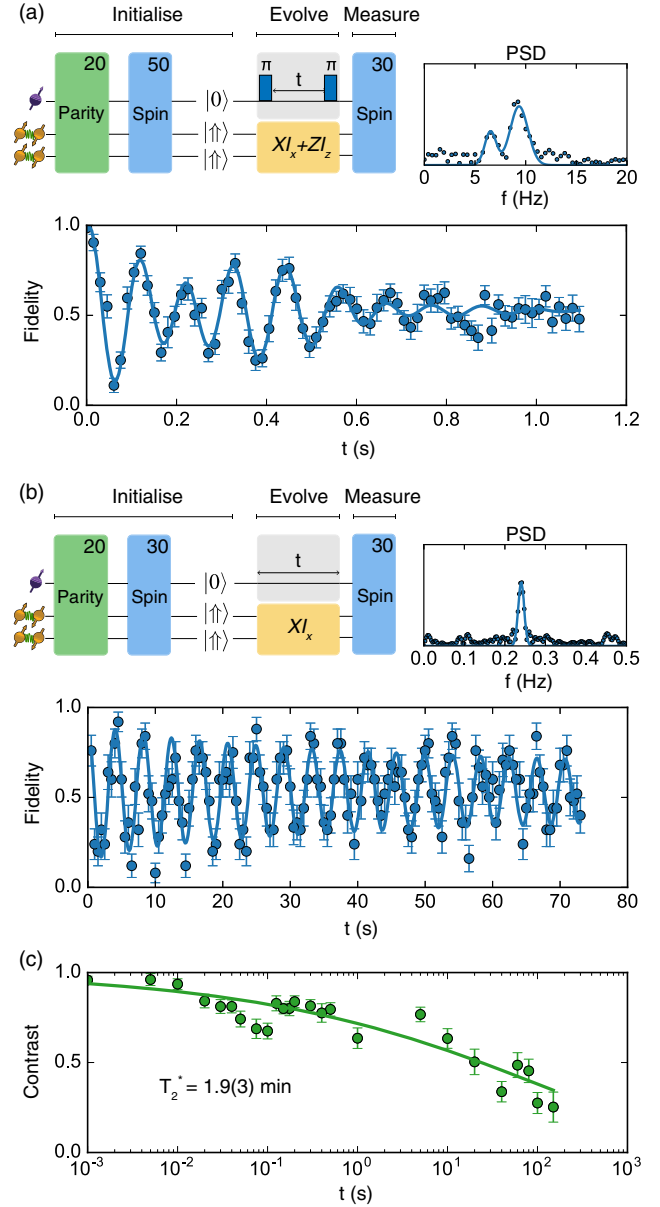


FIG. 3. Coherence of pairs *A* and *B*. (a) Ramsey measurement with the NV in $m_s = -1$. Top left: experimental sequence. Top right: Fourier transform of the signal indicating two frequencies. From the data, we obtain the coupling of the pairs to the NV: $Z_A = 130(1)$ Hz and $Z_B = 91(2)$ Hz. (b) Ramsey measurement with the NV in $m_s = 0$. Top left: experimental sequence. Top right: Fourier transform indicating a single frequency. From the data, we obtain $X = 2080.9900(3)$ Hz. For (a) and (b), a detuning is applied (Appendix B). (c) Each data point corresponds to the amplitude of a Ramsey measurement in $m_s = 0$. A fit yields $T_2^* = 1.9(3)$ min; see Appendix B. The data deviate from a simple exponential decay, indicating that processes beyond pure dephasing contribute to decoherence (Supplemental Sec. I [38]). The error bars represent one standard deviation.

the two spins. The atomic distance between the spins ensures near-complete immunity to noise from distant sources, such as the external magnetic field and the control

signals. The main source of noise is the surrounding ^{13}C spin bath. Hence, $\Delta Z(t)$ can be approximated as a Gaussian distribution with a correlation time τ_c [40,41] and variance $b^2 = \frac{1}{4} \sum_k (A_k^{(1)} - A_k^{(2)})^2$, where $A_k^{(1)}$ ($A_k^{(2)}$) is the dipolar coupling of bath spin k to the first (second) spin of the pair. We calculate the typical effective noise strength $b \sim 10$ Hz by numerically simulating many spin-bath configurations. This is a noise reduction by a factor of approximately 2 due to the decoherence-free subspace (Appendix F).

We first analyze the case of the NV electron spin in $m_s = -1$ [Fig. 3(a)], which enables us to extract the strength of the noise due to the spin bath. Because $X \gg Z \gg \Delta Z(t)$, the Hamiltonian can be approximated as (Supplemental Sec. I [38])

$$H = \left(\omega_{-1} + \frac{Z}{\omega_{-1}} \Delta Z(t) \right) \hat{I}_x, \quad (3)$$

with $\omega_{-1} = \sqrt{X^2 + Z^2}$. Additionally, the NV spin creates a field gradient that suppresses spin flip flops in the bath (a frozen core [4,9]). Therefore, the noise can be treated as quasistatic, and the signal decay is Gaussian [40], as experimentally observed [Fig. 3(a)]. The dephasing time is given by [40]

$$T_2^* = \frac{\omega_{-1}}{Z} \frac{\sqrt{2}}{b}. \quad (4)$$

In this case, the coherence is enhanced by a factor of $(\omega_{-1}/Z) \approx 20$ in addition to the enhancement by the decoherence-free subspace. Finally, inserting the measured dephasing times into Eq. (4) yields noise strengths $b_A = 13.9(2)$ Hz and $b_B = 12.5(4)$ Hz. These values are consistent with the interpair distance and ^{13}C concentration (Appendix F).

Second, we analyze the case with the NV electron spin in $m_s = 0$ [Fig. 3(b)]. Because $X \gg \Delta Z(t)$, the Hamiltonian can be approximated as (Supplemental Sec. I [38]) [41]

$$H = X \hat{I}_x + \frac{\Delta Z^2(t)}{2X} \hat{I}_x. \quad (5)$$

The eigenenergies are now first-order insensitive to $\Delta Z(t)$ as the spin pair forms a clock transition due to the coupling X , a second mechanism that enhances coherence. Note that the clock transition in this system does not require a specific magnetic-field value, as the simultaneous decoherence-free subspace removes the dependence on global magnetic fields.

The decoherence-free subspace and clock transition alone cannot yet explain the observed $m_s = 0$ dephasing time. In particular, for quasistatic or slow noise, the coherence would be limited to approximately 10 s (Supplemental Sec. I [38]). However, the increased coherence, in combination with the lack of a frozen core for

$m_s = 0$, unlocks a new regime in which the nuclear-spin bath fluctuations become relatively fast ($\tau_c \ll X/b^2$). A mathematically equivalent Hamiltonian is analyzed theoretically by Dobrovitski *et al.* [41]. The resulting time constant is

$$T_2^* = \frac{4X^2}{b^4 \tau_c}. \quad (6)$$

The dependence on the correlation time τ_c reveals a third mechanism, similar to motional narrowing [41], that further enhances the coherence. Inserting the parameters obtained from the $m_s = -1$ measurement and a typical value for $\tau_c \sim 0.1$ s [16], inhomogeneous dephasing times of approximately 100 s are predicted. Together, these three mechanisms thus provide an explanation for the observed dephasing times.

VI. COHERENCE OF PAIR C

To further analyze the different physical regimes that play a role, we investigate pair *C* (Fig. 1). Because $Z \gg X$, the dynamics are different and the clock transition can be switched on ($m_s = 0$) and off ($m_s = -1$) (Supplemental Sec. I [38]). We develop complete control, initialization, and single-shot readout of such pairs in Appendix D.

For evolution under $m_s = 0$, the situation is similar to pairs *A* and *B*. We find $T_2^* = 0.6(1)$ s, which is reduced compared to pairs *A* and *B*, because the smaller coupling X makes the clock transition less effective (Appendix D). Additionally, similar values obtained for spin echo [$T_2 = 0.7(1)$ s] and relaxation measurements [$T_1 = 0.9(2)$ s] indicate that relaxation plays a role in limiting the coherence (Supplemental Sec. I [38]). For $m_s = -1$, a frozen core is formed and the clock transition is turned off, so that the noise $\Delta Z(t)$ affects the eigenfrequencies linearly. We find $T_2^* = 18(1)$ ms with Gaussian decay, indicating quasistatic noise [40], which is consistent with spin echo [$T_2 = 0.3(2)$ s $\gg T_2^*$] and relaxation measurements ($T_1 \gg 1$ s) (Appendix D). In this case, there is no significant coherence protection, and the results are similar to individual ^{13}C spins [4].

VII. ENTANGLING TWO SPIN-PAIR QUBITS

Finally, we demonstrate the potential of the spin pairs as qubits by demonstrating an entangled state of pair *A* and pair *B*. We create entanglement through subsequent projective measurements of the $\sigma_y \sigma_y$ and $\sigma_z \sigma_z$ pseudospin parity [Fig. 4(a)]. We herald on outcomes $\langle \sigma_y \sigma_y \rangle = +1$ and $\langle \sigma_z \sigma_z \rangle = -1$, so that the resulting state is $(1/\sqrt{2})(|\uparrow\downarrow\rangle + |\downarrow\uparrow\rangle)$. This state is a four-spin-entangled state $(1/\sqrt{2})(|\uparrow\downarrow\downarrow\uparrow\rangle + |\downarrow\uparrow\uparrow\downarrow\rangle)$ that encodes two qubits of information in two long-lived pseudospin states.

To characterize the resulting state, we first measure parity oscillations by varying the evolution time t

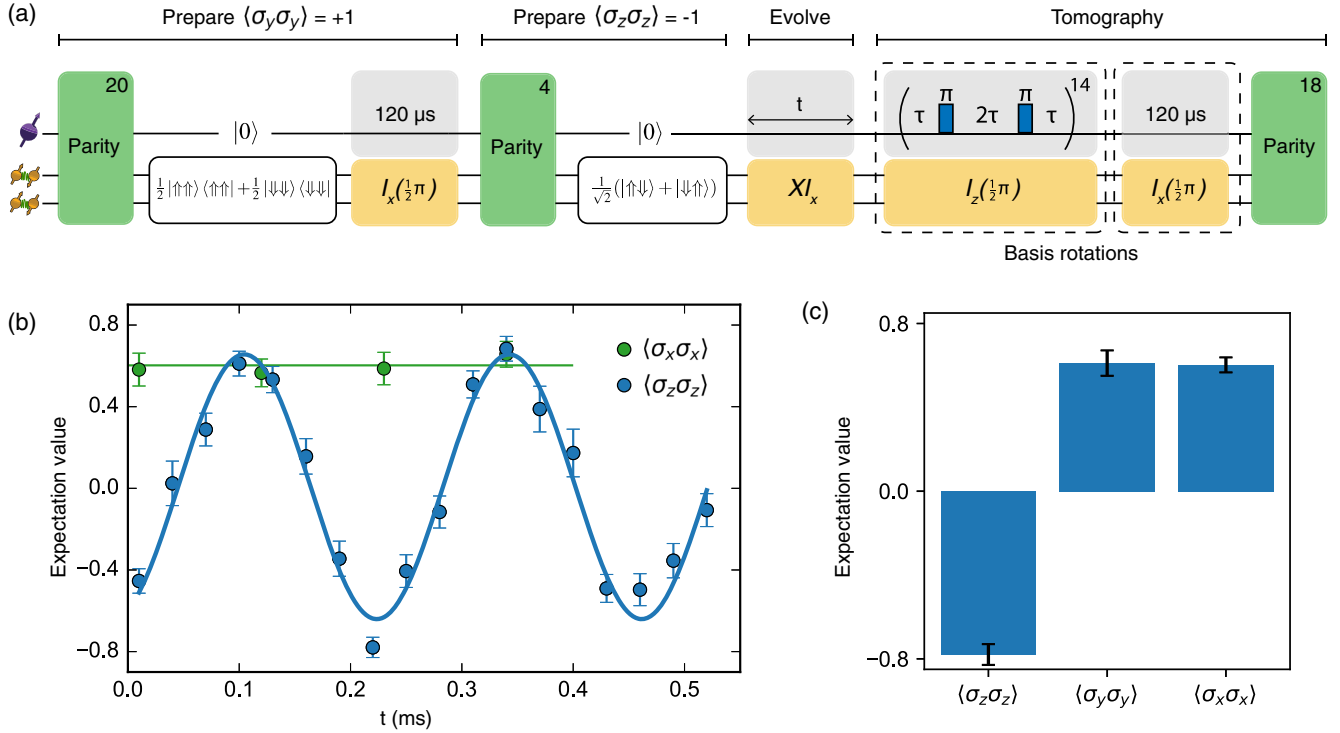


FIG. 4. Entanglement of pairs *A* and *B*. (a) Experimental sequence. We prepare the entangled state $(1/\sqrt{2})(|\uparrow\downarrow\rangle + |\downarrow\uparrow\rangle)$ by consecutively measuring $\langle\sigma_y\sigma_y\rangle$ and $\langle\sigma_z\sigma_z\rangle$. We herald on the +1 ($> 14/20$ counts) and -1 ($< 1/4$ counts) outcomes in the initialization steps. Final operators are measured through optional basis rotations (dashed boxes) and a $\langle\sigma_z\sigma_z\rangle$ parity measurement. $I_{x/z}(\phi)$ stands for a rotation around x/z by an angle ϕ . (b) Parity oscillations show a frequency of 4.20(4) kHz (approximately $2X$). For $\langle\sigma_x\sigma_x\rangle$, no oscillation is observed, as the pseudospin eigenstates are along x . (c) Measurement of the three nonzero operators of the entangled state. The state fidelity is $F = (1 - \langle\sigma_z\sigma_z\rangle + \langle\sigma_y\sigma_y\rangle + \langle\sigma_x\sigma_x\rangle)/4 = 75(2)\%$. We use $t = 225 \mu\text{s}$ for measuring $\langle\sigma_z\sigma_z\rangle$ and $t = 105 \mu\text{s}$ for measuring $\langle\sigma_y\sigma_y\rangle$. The results are not corrected for readout infidelity, and the error bars represent one standard deviation.

[Fig. 4(a)]. The observed frequency is 4.20(4) kHz, which equals $2X$, as expected [Fig. 4(b)]. To determine the state fidelity, we measure the pseudospin parity operators $\langle\sigma_x\sigma_x\rangle$, $\langle\sigma_y\sigma_y\rangle$, and $\langle\sigma_z\sigma_z\rangle$. We realize the required single-qubit rotations through waiting times (for x rotations) and dynamical decoupling sequences with the NV spin in an eigenstate (for z rotations) [Fig. 4(a)]. Figure 4(c) shows the resulting expectation values, which yield a fidelity $F = 0.75(2)$, confirming entanglement ($F > 0.5$) [42]. This result highlights the high-fidelity initialization, control, and nondestructive measurements realized.

VIII. CONCLUSION

In conclusion, we have developed complete control over multiple nuclear-spin pairs. These spin pairs provide inherently long-lived quantum states due to a combination of three physical phenomena: a decoherence-free subspace, a clock transition, and a variant of motional narrowing. This inherent coherence protection makes spin pairs promising systems for a variety of applications, such as robust memories for optically connected quantum networks [18–20,43] and memory-enhanced sensing [44–49].

For quantum networks, the long coherence time and small effective coupling to the NV electron spin (a few hertz) might enable faithful storage of quantum states during the probabilistic generation of NV-NV entanglement through optical channels. Such a robust memory is a key requirement for progressing toward larger-scale networks based on defect spins [19,43,50]. For sensing, a hybrid system consisting of a sensitive quantum sensor (e.g., the NV electron spin) in conjunction with a robust quantum memory can increase sensitivity and enhance sensor properties [44–49].

Furthermore, the presented methods might be extended to electron spin pairs, where greater control speeds are possible, and provide new opportunities for the magnetic imaging of spin systems through spin-spin interactions [12]. Further improved control over the spin pairs might be realized by using tailored decoupling sequences [51–58]. Such long-lived nuclear spin pairs are available for most NV centers (Appendix H) and are present in a variety of other materials. Therefore, our results reveal a new, promising, and abundantly available resource for quantum science and technology.

ACKNOWLEDGMENTS

We thank V. V. Dobrovitski and L. M. K. Vandersypen for valuable discussions. This work was supported by the Netherlands Organisation for Scientific Research (NWO/OCW) through a Vidi grant and as part of the Frontiers of Nanoscience (NanoFront) program. This project has received funding from the European Research Council (ERC) under the European Unions Horizon 2020 research and innovation program (Grant Agreement No. 852410). This project (QIA) has received funding from the European Unions Horizon 2020 research and innovation program under Grant Agreement No. 820445. This work was supported by the Netherlands Organisation for Scientific Research (NWO/OCW) as part of the Quantum Software Consortium program (Project No. 024.003.037/3368). B. P. acknowledges financial support through a Horizon 2020 Marie Skłodowska-Curie Actions global fellowship (COHESiV, Project No. 840968) from the European Commission.

APPENDIX A: SAMPLE AND SETUP

The experiments are performed on a naturally occurring NV center in a cryogenic confocal microscope (3.7 K). The diamond is homoepitaxially grown using chemical vapor deposition and cleaved along the $\langle 111 \rangle$ axis (Element Six). There is a natural abundance (1.1%) of ^{13}C . The NV center is selected on the absence of strongly coupled ^{13}C spins exceeding approximately 500 kHz hyperfine coupling but without any other criteria on the spin environment or spin pairs.

The NV electron spin has a dephasing time of $T_2^* = 4.9(2) \mu\text{s}$ and a spin echo time of $T_2 = 1.182(5) \text{ ms}$. The electron relaxation ($T_1 > 1 \text{ h}$) at this temperature is negligible [11]. We measure the NV spin state in a single shot using spin-selective optical readout [16]. The readout fidelities are 0.905(2) [0.986(2)] for the $m_s = 0$ ($m_s = -1$) state with an average fidelity of $F = 0.946(1)$. The dynamical decoupling sequences follow the XY8 scheme to mitigate pulse errors [59]. The NV studied in this work is the same NV studied in Aboeih *et al.* [12]. However, the ^{13}C spins that constitute the pairs studied in this work are not part of the 27 spins that are found in Ref. [12].

APPENDIX B: DATA ANALYSIS

1. Fit functions

The Ramsey data in Fig. 3(a) ($m_s = -1$) are fitted to

$$F(t) = a + \exp[-(t/T)^n] [A \cos(2\pi f_A t + \phi_A) + B \cos(2\pi f_B t + \phi_B)]. \quad (\text{B1})$$

We obtain $T = 0.53(4) \text{ s}$, $n = 2.1(4)$, $f_A = 9.07(6) \text{ Hz}$, and $f_B = 7.0(1) \text{ Hz}$ (measured with a 10-Hz detuning with respect to 2086 Hz). Using $f = \sqrt{X^2 + Z^2}$ and

$X = 2080.9900(3) \text{ Hz}$, the values for f_A and f_B yield $Z_A = 130(1) \text{ Hz}$ and $Z_B = 91(2) \text{ Hz}$, respectively. The observed shape of the decay [$n = 2.1(4)$] is in agreement with the predicted Gaussian ($n = 2$) decay for quasistatic noise (Supplemental Sec. I [38]).

To extract the dephasing times, we fit the Fourier transform in Fig. 3(a) to

$$F(f) = a + A \exp[-(f + f_A)^2/2\sigma_A^2] + B \exp[-(f + f_B)^2/2\sigma_B^2]. \quad (\text{B2})$$

We find $\sigma_A = 0.88(6) \text{ Hz}$ and $\sigma_B = 0.57(9) \text{ Hz}$, which gives $T_{2,A}^* = 1/(\sqrt{2}\pi\sigma_A) = 0.26(2) \text{ s}$ and $T_{2,B}^* = 0.39(6) \text{ s}$.

The Ramsey data in Fig. 3(b) ($m_s = 0$) are fitted to

$$F(t) = \exp[-(t/T)^n] \cos(2\pi f t + \phi). \quad (\text{B3})$$

We obtain $T = 98(44) \text{ s}$, $n = 0.5(4)$, and $f = 0.2400(3) \text{ Hz}$ (measured with a 0.25-Hz detuning with respect to 2081 Hz). Therefore, we obtain $X = 2080.9900(3) \text{ Hz}$. Note that the precise value obtained for X deviates from simple theoretical estimates and is analyzed in Supplemental Sec. VII [38]. The Fourier transform is fitted to

$$F(f) = a + A \exp[-(f + f_0)^2/2\sigma_0^2]. \quad (\text{B4})$$

We obtain $f_0 = 0.2402(3) \text{ Hz}$ and $\sigma_0 = 0.0074(3) \text{ Hz}$.

The data in Fig. 3(c) are fitted to $\exp[-(t/T)^n]$, obtaining $T = 1.9(3) \text{ min}$ and $n = 0.23(2)$. Note that n deviates from the simple exponential decay ($n = 1$) associated to Eq. (6), indicating that other effects beyond pure dephasing contribute to the decoherence (Supplemental Sec. I [38]).

The data in Fig. 3 as well as the data in Fig. 7 are corrected for NV ionization.

2. Error analysis

All error bars on data points represent one standard deviation. The error on data involving single-shot readout of (the parity of) nuclear spin pairs is given by a binomial error:

$$\sigma = \sqrt{\frac{p(1-p)}{n}}, \quad (\text{B5})$$

where p is the success probability in a Bernoulli process and n is the number of trials. When a data point consists of m independent datasets, the individual errors are added in quadrature:

$$\sigma = \frac{1}{m} \sqrt{\sum_i \sigma_i^2}. \quad (\text{B6})$$

In Fig. 3(c), the error bars are instead given by the fit error on the amplitude of the underlying Ramsey measurements.

APPENDIX C: PSEUDOSPIN HAMILTONIAN

The Hamiltonian for two ^{13}C spins in the vicinity of an NV center in the interaction picture with respect to the electron energy splitting and under the secular approximation can be written as

$$H = \omega_L I_z^{(1)} + \omega_L I_z^{(2)} + m_s \mathbf{A}^{(1)} \cdot \mathbf{I}^{(1)} + m_s \mathbf{A}^{(2)} \cdot \mathbf{I}^{(2)} + H_D, \quad (\text{C1})$$

where $\omega_L = \gamma_c B$ is the ^{13}C spin Larmor frequency, with γ_c the ^{13}C gyromagnetic ratio. B is the magnetic field along the

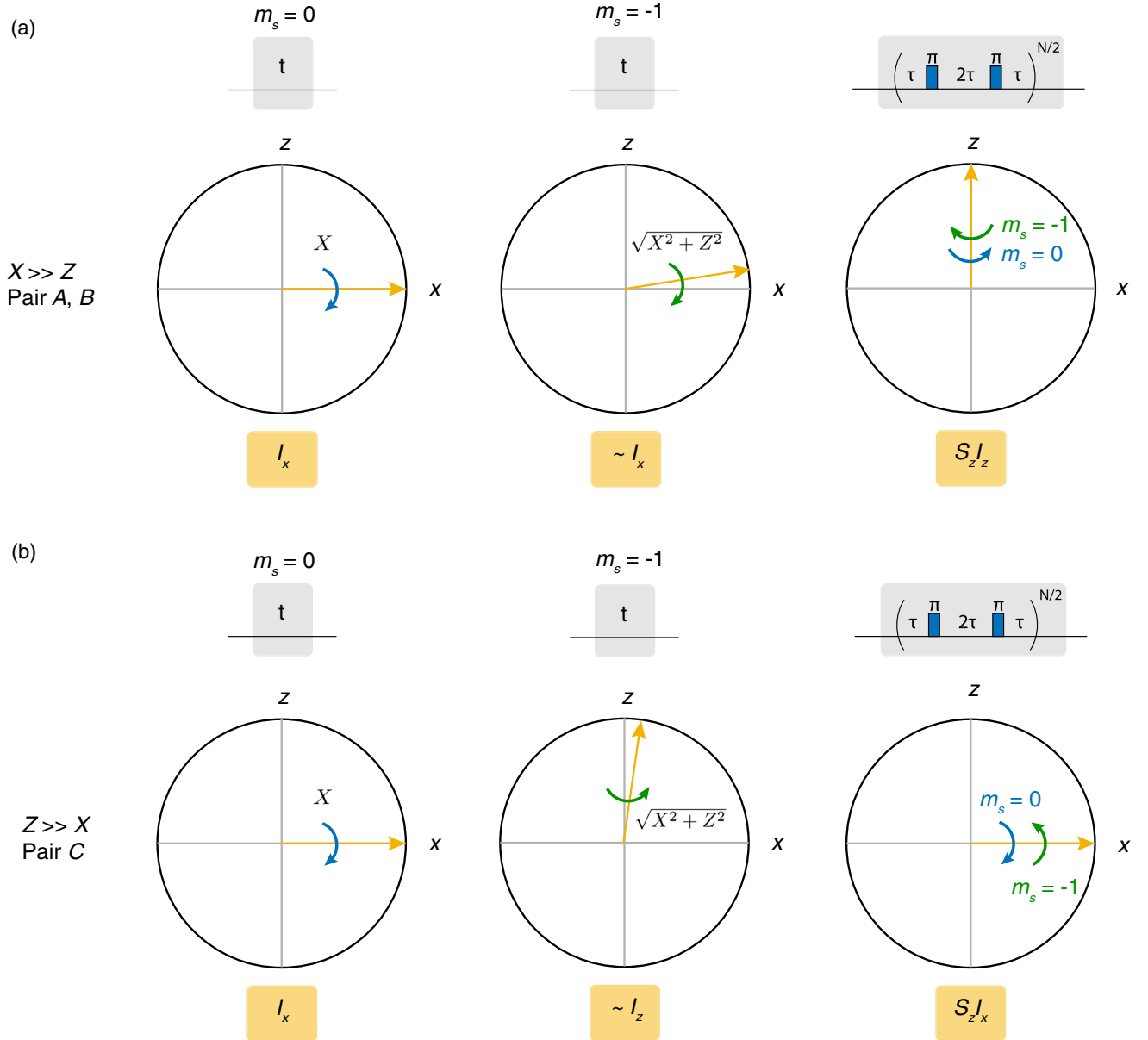


FIG. 5. Overview of pair pseudospin dynamics during various sequences on the NV electron spin. (a) Pseudospin dynamics of pairs with $X \gg Z$ (pairs A and B). The top row indicates the sequence performed on the NV electron spin, the middle row indicates the corresponding pair dynamics in the XZ plane of the pseudospin Bloch sphere, and the bottom row indicates the effective pseudospin Hamiltonian term under that sequence. For the left two columns, the rotation frequencies are given inside the Bloch spheres. From left to right, the sequences are free evolution in $m_s = 0$ and $m_s = -1$ and a dynamical decoupling sequence with τ resonant, i.e., $2\tau = \pi/\sqrt{X^2 + (Z/2)^2}$. Rotations that are unconditional on the NV electron spin state can be obtained by setting $\tau = \pi/\sqrt{X^2 + (Z/2)^2}$ (unconditional z rotation) and by setting τ far off resonant (unconditional x rotation), but these are not shown or used here. Note that the z -rotation frequency depends on the hyperfine field difference Z , so that pairs A and B can, in principle, be controlled individually. (b) Pseudospin dynamics of pairs with $Z \gg X$ (pair C). Like above, z and x rotations that are unconditional on the NV electron-spin state can be obtained by setting different values for τ (not shown). Together, these operations enable universal control of the system consisting of the three pseudospins and the NV center.

NV axis. $\mathbf{I}^{(i)}$ are the spin- $\frac{1}{2}$ operators acting on spin i , $m_s = \{-1, 0, +1\}$ are the NV electron spin states, and $\mathbf{A}^{(i)} = [A_x, A_y, A_z]$ is the NV- ^{13}C hyperfine interaction vector of spin i . H_D is the dipolar interaction between two ^{13}C spins. Throughout the paper, all units in equations (X , Z , b , etc.) are in angular frequency. For a large magnetic field compared to the dipolar (X) and hyperfine couplings ($A^{(1)}, A^{(2)}$), H_D can be written as

$$H_D = X(3I_z^{(1)}I_z^{(2)} - \mathbf{I}^{(1)} \cdot \mathbf{I}^{(2)}), \quad (\text{C2})$$

$$X = \frac{\mu_0 \gamma_c \gamma_c \hbar}{8\pi |\mathbf{r}_{12}|^3} (1 - 3\cos^2\theta_{12}), \quad (\text{C3})$$

where μ_0 is the vacuum permeability, \mathbf{r}_{12} is the vector between the two ^{13}C atoms, and θ_{12} is the angle between the magnetic-field axis and the pair axis. Since $\omega_L = \gamma_c B = 432.140$ kHz is large compared to the dipolar (X) and hyperfine couplings ($A^{(1)}, A^{(2)}$), the antiparallel states $|\uparrow\downarrow\rangle$ and $|\downarrow\uparrow\rangle$ form an isolated subspace in which we define a pseudospin $\frac{1}{2}$ as $|\uparrow\rangle = |\uparrow\downarrow\rangle$ and $|\downarrow\rangle = |\downarrow\uparrow\rangle$ [11,13,14,37]. The Hamiltonian in this subspace is given by [13,37]

$$H = X\hat{I}_x + m_s Z\hat{I}_z. \quad (\text{C4})$$

Z originates from the difference of the hyperfine couplings of the two spins to the NV electron spin and is given by [37]

$$Z = Z_{\parallel} + Z_{\perp} = A_{\parallel}^{(1)} - A_{\parallel}^{(2)} + \frac{(A_{\perp}^{(1)})^2 - (A_{\perp}^{(2)})^2}{\gamma_c B}, \quad (\text{C5})$$

where $A_{\parallel}^{(i)} = A_z^{(i)}$ and $A_{\perp}^{(i)} = \sqrt{(A_x^{(i)})^2 + (A_y^{(i)})^2}$ for spin i of the pair.

APPENDIX D: PAIR C CONTROL, COHERENCE, AND RELAXATION

Pair C has a dipolar coupling $X = 188.33(2)$ Hz and a hyperfine difference $Z = 2802(2)$ Hz. Therefore, $Z \gg X$, in contrast to pairs A and B for which $X \gg Z$. This changes the dynamics in two ways. First, for $m_s = -1$, Z is the dominant term in the pair frequency $\omega_{-1} = \sqrt{X^2 + Z^2}$ and, thus, sets the location of the resonance in Fig. 1(b). Second, the effective NV-pair interaction during the dynamical decoupling sequence becomes $\hat{S}_z \hat{I}_x$ [11] (Fig. 5).

We implement two types of projective measurements on pair C (see Fig. 6). The spin measurement sequence distinguishes the pseudospin states $(1/\sqrt{2})(|\uparrow\rangle \pm |\downarrow\rangle)$. The parity measurement sequence distinguishes between the parallel ($|\uparrow\uparrow\rangle, |\downarrow\downarrow\rangle$) and antiparallel ($|\uparrow\downarrow\rangle, |\downarrow\uparrow\rangle$)

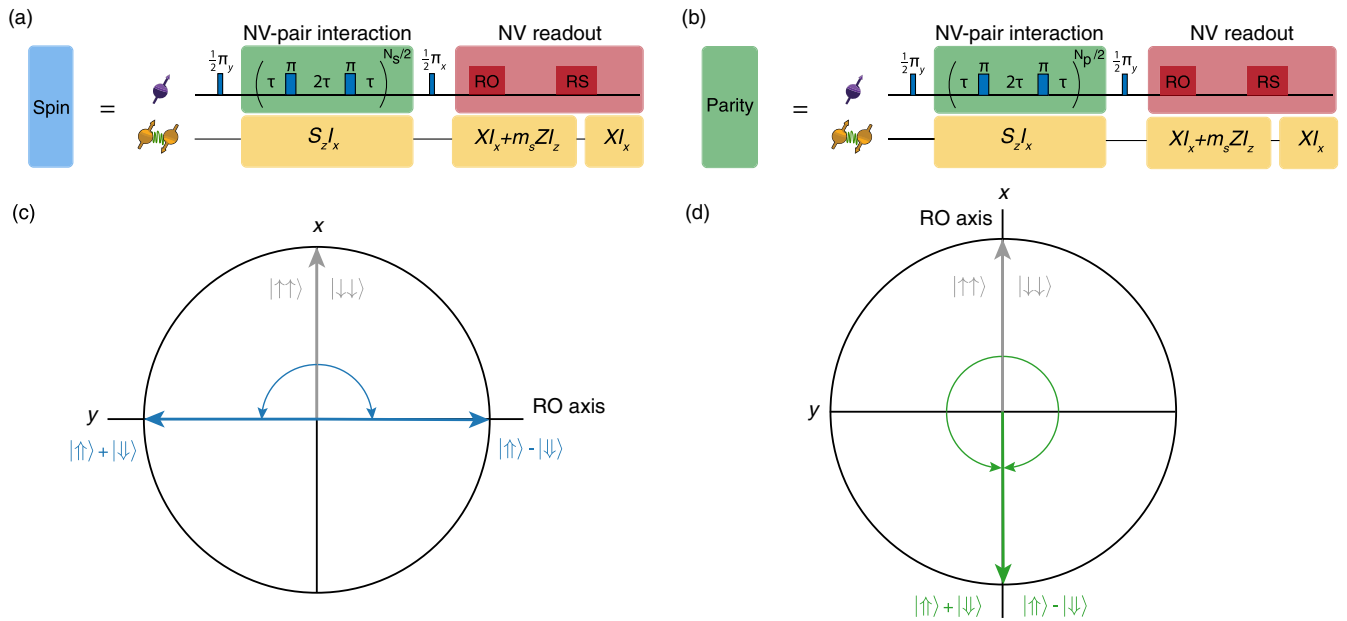


FIG. 6. Projective spin and parity measurements for pair C . (a) Sequence to measure the spin state of pair C . The NV starts in $m_s = 0$. Because $Z \gg X$, the effective interaction between the NV spin and pseudospin is $\hat{S}_z \hat{I}_x$. During the NV readout (RO) and reset (RS), the NV can spend an unknown time in $m_s = -1$ which causes dephasing of the pair spin. Additionally, pair C undergoes a deterministic z rotation for any known time spent in $m_s = -1$. To minimize these effects, we use a fast readout and reset. $N_s = 8$. (b) Sequence to measure the parity of the two spins that make up pair C . Note that in this case the timing of the sequence is unimportant, as evolution in $m_s = -1$ or $m_s = 0$ does not change the parity. $N_p = 14$. (c) XY plane of the NV Bloch sphere during the NV-pair interaction in (a). The NV picks up a positive or negative phase depending on the x projection of the pair pseudospin and no phase when the pair is in the parallel subspace. (d) XY plane of the NV Bloch sphere during the NV-pair interaction in (b).

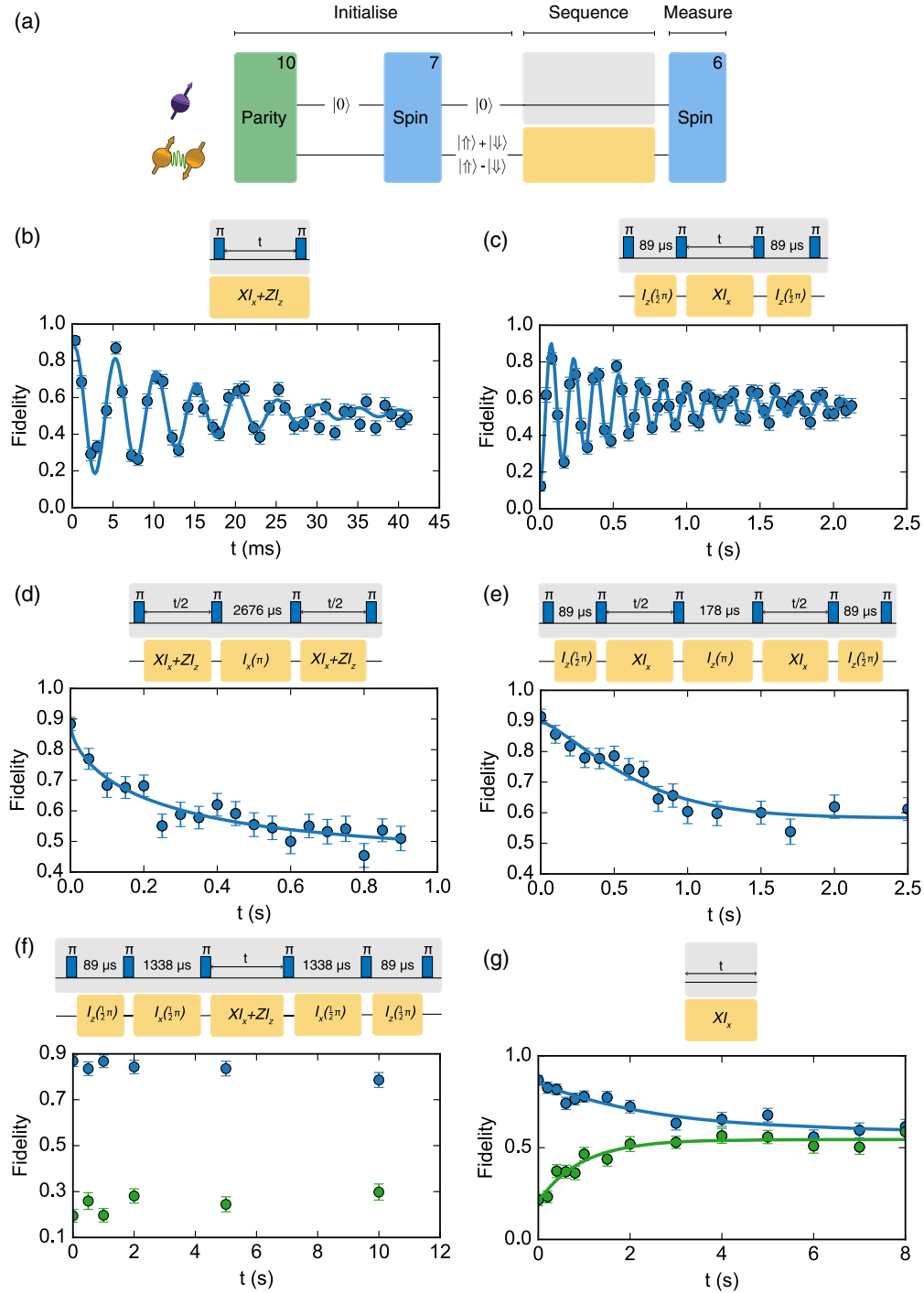


FIG. 7. Coherence and relaxation of pair C. (a) Measurement sequence. First, we use ten parity readouts to herald the pair in the antiparallel subspace (condition $> 7/10$). Then, we use seven spin readouts to initialize the pair in $(1/\sqrt{2})(|\uparrow\rangle + |\downarrow\rangle)$ ($> 4/7$, blue data) or $(1/\sqrt{2})(|\uparrow\rangle - |\downarrow\rangle)$ ($< 3/7$, green data). The various evolution sequences are given as insets in (b)–(g). Finally, six spin readouts are used to read out the spin state. (b) and (c) are fitted to $F(t) = a + Ae^{-(t/T)^n} \cos(2\pi ft + \phi)$ and (d), (e), and (g) to $F(t) = a + Ae^{-(t/T)^n}$. (b) Ramsey measurement in $m_s = -1$. $T_2^* = 0.018(1)$ s, $n = 1.4(2)$, and $f = 2808(1)$ Hz (measured with a 200-Hz detuning with respect to 2807 Hz). (c) Ramsey measurement in $m_s = 0$. $T_2^* = 0.6(1)$ s, $n = 0.7(1)$, and $f = 188.33(2)$ Hz (measured with a 5-Hz detuning with respect to 186.8 Hz). (d) Spin echo measurement in $m_s = -1$. $T_2 = 0.3(2)$ s and $n = 0.6(2)$. (e) Spin echo measurement in $m_s = 0$. $T_2 = 0.7(1)$ s and $n = 1.3(3)$. (f) Relaxation measurement in $m_s = -1$. $T_1 \gg 1$ s. (g) Relaxation measurement in $m_s = 0$. $T_1 = 3.6(7)$ s and $n = 0.8(2)$ for the blue data $[(1/\sqrt{2})(|\uparrow\rangle + |\downarrow\rangle)]$. $T_1 = 0.9(2)$ s and $n = 1.0(2)$ for the green data $[(1/\sqrt{2})(|\uparrow\rangle - |\downarrow\rangle)]$. The relaxation times are different for the two eigenstates, indicating a mechanism that depends on whether the state is a singlet or triplet.

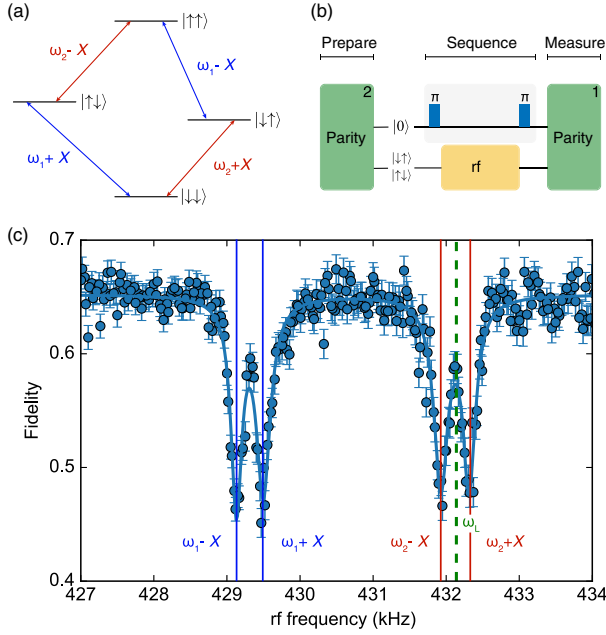


FIG. 8. Spectroscopy and control of the complete pair Hilbert space. (a) Level diagram for pair C with the electron spin in $m_s = -1$. ω_1 (ω_2) is the frequency associated to the first (second) spin of the pair with the NV in $m_s = -1$. (b) Sequence to reveal the transitions between the subspaces. First, the pair is initialized in the antiparallel subspace through a parity measurement, then an rf pulse with variable frequency with the NV in $m_s = -1$ is applied, and finally the subspace population is measured using another parity measurement. If the frequency of the rf pulse is resonant with a single-spin transition, the spin pair changes its subspace. (c) Measurement result. Four transitions are observed corresponding to the marked transitions in (a). The green dashed line corresponds to the bare Larmor frequency $\omega_L = 432.140$ kHz. We fit the data to four Lorentzians and extract $\omega_1 = 429.314(5)$ kHz and $\omega_2 = 432.122(7)$ kHz. For the left (right) dips, we also obtain $X = 184(3)$ [194(4)] Hz. These results corroborate the assignment of the signals to ^{13}C pairs and enable complete control over the full pair state.

subspaces of the pair. We obtain high-fidelity initialization and readout by repeatedly applying these sequences (Supplemental Secs. V and VI [38]).

For spin pairs with $Z \gg X$, the timing of repetitions is complicated by the fact that the $m_s = 0$ and $m_s = -1$ evolution frequencies and eigenstates differ significantly. Here, we mitigate this by minimizing the NV readout time (approximately $5 \mu\text{s}$) and applying a fast reset of the NV spin, so that the potential time spent in $m_s = -1$ is small. Because the states that the measurement projects onto $[(1/\sqrt{2})(|\uparrow\rangle \pm |\downarrow\rangle)]$ are eigenstates of the $m_s = 0$ evolution, there is no timing requirement after resetting the NV, and we simply concatenate subsequent measurements.

For pairs A and B ($X \gg Z$), we use free evolution and dynamical decoupling sequences to realize universal single-qubit control for the pseudospins (Figs. 4 and 5). For pair C ($Z \gg X$), all single-qubit operations can be obtained

by letting the system evolve freely. Evolution with the NV electron spin in $m_s = 0$ implements a rotation around the x axis, and evolution under $m_s = -1$ realizes a rotation around the z axis. Note that the z -axis rotation is approximate, as Z is finite. In principle, this can be corrected for, but this is not done here. We use the pair C control to measure the pseudospin dephasing time T_2^* , the spin echo time T_2 , and the relaxation time T_1 in both NV electron spin states; see Fig. 7.

APPENDIX E: SPECTROSCOPY AND CONTROL OF THE FULL HILBERT SPACE

Most of the work presented is focused on initializing, controlling, and measuring the states in the antiparallel subspace of spin pairs, i.e., $|\uparrow\downarrow\rangle$ and $|\downarrow\uparrow\rangle$. In Fig. 8, we demonstrate that the entire Hilbert space of the spin pairs can be controlled by rf driving the single-spin-flip transitions of pair C .

The single-spin transition frequencies are $\omega_1 = 429.314(5)$ kHz and $\omega_2 = 432.122(7)$ kHz [Fig. 8(a)]. Since the frequency of a single-spin transition in $m_s = -1$ is $\omega \approx \omega_L - A_{\parallel}$, this yields $A_{\parallel}^{(1)} = 2826(5)$ Hz and $A_{\parallel}^{(2)} = 18(7)$ Hz. Note that these values assume that A_{\perp} is of similar magnitude, so that it can be neglected. The frequencies observed are consistent with the characteristic ^{13}C frequencies ($\omega_L = 432.140$ kHz), further corroborating our assignment of ^{13}C - ^{13}C pairs as the source of the signals.

These results also demonstrate selective initialization, control, and measurement of an individual carbon spin with negligible coupling to the NV by using its coupling to neighboring spins. Spin 2 couples negligibly to the NV [18(7) Hz], so that it overlaps in precession frequency with most of the spin bath. Nevertheless, it can be initialized and controlled selectively by using the NV to directly detect its flip flops with spin 1 (i.e., pseudospin dynamics).

APPENDIX F: DECOHERENCE-FREE SUBSPACE AND SPIN BATH NOISE

The noise $\Delta Z(t)$ on a spin pair originates from the surrounding ^{13}C spins. As a pair is sensitive only to field gradients (a decoherence-free subspace), distant external noise sources can generally be neglected. There are k bath spins that each create a field difference $A_k^{(1)} - A_k^{(2)}$ on the pair [Fig. 9(a)]. We model $\Delta Z(t)$ as an Ornstein-Uhlenbeck process with a variance $b^2 = \frac{1}{4} \sum_k (A_k^{(1)} - A_k^{(2)})^2$. The question that we address in this section is what b is for typical spin baths.

We numerically generate 10^5 different baths (1.1% ^{13}C abundance) surrounding a pair [Figs. 9(b) and 9(c)] or a single spin [Fig. 9(d)] in a volume of $15 \times 15 \times 15$ unit cells. For each bath, we calculate $b^2 = \frac{1}{4} \sum_k (A_k^{(1)} - A_k^{(2)})^2$ but exclude spins with $|A_k^{(1)}| > 50$ Hz or $|A_k^{(2)}| > 50$ Hz;

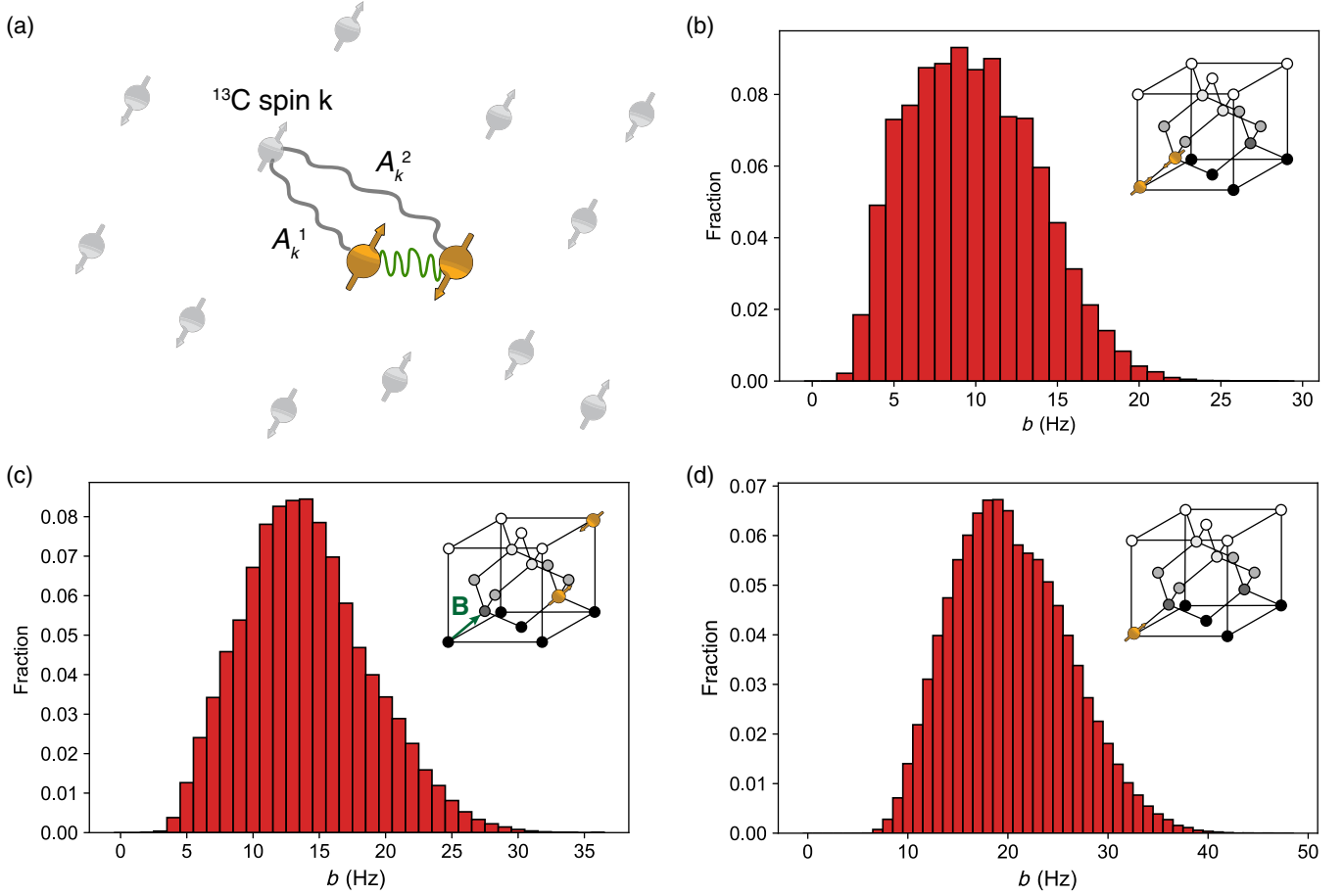


FIG. 9. Distributions of the noise strength b for typical baths. (a) Schematic of the situation. A pair is surrounded by k bath spins that each create a magnetic-field difference $A_k^{(1)} - A_k^{(2)}$ on the pair. Assuming Gaussian noise, we obtain b from $b^2 = \frac{1}{4} \sum_k (A_k^{(1)} - A_k^{(2)})^2$. (b)–(d) Distribution of b for 10^5 generated baths for the parameters of pairs A and B (b), for the parameters of pair C (c), and for a single spin (d). Strongly coupled spins ($|A_k^{(1)}| > 50$ Hz or $|A_k^{(2)}| > 50$ Hz) are excluded.

i.e., we exclude strongly coupled spins for which the system would not be a well-defined spin pair anymore. The expectation is that the closer the spins of the pair are, the more correlated the noise and the smaller b is.

The result for a nearest-neighbor pair oriented along the magnetic field (like pair A or B) is shown in Fig. 9(b). We find a mean of 10 Hz and a standard deviation of 4 Hz. For the parameters of pair C [Fig. 9(c)], we find a mean of 14 Hz and a standard deviation of 5 Hz. Last, for an individual ^{13}C spin [Fig. 9(d)], we find a mean of 20 Hz and a standard deviation of 6 Hz. A decrease in the effective noise is observed for the pairs compared to an individual spin. Furthermore, the closer the pair spins are, the smaller the effective noise is.

APPENDIX G: DECOHERENCE-FREE SUBSPACE AND EXTERNAL NOISE

The decoherence-free subspace makes pairs nearly immune to noise from distant sources. In this section, we consider the effect of two such external sources. For

single ^{13}C spins in the same sample, typical inhomogeneous dephasing times of 10 ms are observed [4], which sets a bound on the noise strength. If we take the extreme case that all noise comes from an external source, i.e., not from the spin bath, this gives an upper limit of the noise magnitude $b = 1/\sqrt{2\pi T_2^*} = 22.5$ Hz. Since we are interested in an order-of-magnitude estimate, we take $b \sim 10^2$ Hz, corresponding to magnetic-field fluctuations of $\delta B \sim 10^{-5}$ T. Now we consider that these fluctuations originate from either the on-chip MW line that we use to apply microwaves or from the external magnets that we use to apply a magnetic field.

1. Microwave line

We approximate the microwave line as an infinite wire that generates a field at a distance r from the wire of magnitude $B(r) = \mu_0 I / 2\pi r$, where μ_0 is the vacuum permeability and I the current through the wire. Given $r \sim 10 \mu\text{m}$ and $\delta B \sim 10^{-5}$ T, we obtain $I = 2\pi r \delta B / \mu_0 \sim 10^{-4}$

A. Now we turn to the effect of this noise on a decoherence-free subspace formed by a ^{13}C pair. The positions of the pair spins are $r_a = 10 \mu\text{m}$ and $r_b = 10 \mu\text{m} + a_0$, where for a_0 we take a conservative value of approximately 10^{-9} m. Given $I = 10^{-4}$ A, the MW line adds a field difference to the decoherence-free subspace of $\Delta B = B(r_a) - B(r_b) = [(\mu_0 I)/2\pi][(1/r_a) - (1/r_b)] \sim 10^{-10}$ T. That corresponds to approximately 10^{-3} Hz, which has a negligible effect on the coherence.

2. Magnet

The external magnetic field comes from a cylindrical permanent magnet. We calculate the effect of that field (approximately 0.04 T) on the decoherence-free subspace of a pair. From the above, we know that the maximum field fluctuations are on the order of $\delta B \sim 10^{-5}$ T. We consider a magnet with an NV-magnet distance $r \sim 10^{-2}$ m, the radius of the magnet $R = 5$ mm, the length $L = 5$ mm, and the remanence field $B_r = 1.5$ T. To calculate the magnetic field at r , we use

$$B(r) = \frac{B_r}{2} \left(\frac{L+r}{\sqrt{R^2 + (L+r)^2}} - \frac{r}{\sqrt{R^2 + r^2}} \right). \quad (\text{G1})$$

At $r \sim 10^{-2}$ m, the magnetic field is approximately 0.04 T. The expected effect of the permanent field on the decoherence-free subspace is then $B(r_a) - B(r_b) \sim 10^{-8}$ T or 10^{-1} Hz. We use $r_a = 1$ cm and $r_b = 1$ cm + a_0 , where for a_0 we take a conservative value of 10^{-9} m. This is a constant field difference (cf. Z) added to the pair. However, the field fluctuations are $\delta B \sim 10^{-5}$ T, more than 3 orders of magnitude less than the permanent field of approximately 0.04 T. The influence of δB on the decoherence-free subspace is, therefore, < 1 mHz, which has a negligible effect on the coherence.

APPENDIX H: EXPECTED NUMBER OF NEAREST-NEIGHBOR PAIRS PER NV

In this section, we address how many nearest-neighbor pairs with similar Z as pairs A and B one would expect surrounding a typical NV center. To that end, we generate 10^4 different ^{13}C baths with 1.1% abundance surrounding an NV center in a volume of $15 \times 15 \times 15$ diamond unit cells. For every generated bath, we look for the nearest-neighbor pairs along the magnetic-field axis and calculate the hyperfine field difference Z due to the NV, assuming a dipolar NV- ^{13}C interaction. Then, we estimate a controllable region of $50 < Z < 500$ Hz. The upper bound comes from the required condition $X \gg Z$, and the (approximate) lower bound is a limit due to the detrimental effect of electron dephasing for a large number of dynamical decoupling pulses. Additionally, for smaller Z , resolving a pair from the background bath of pairs with

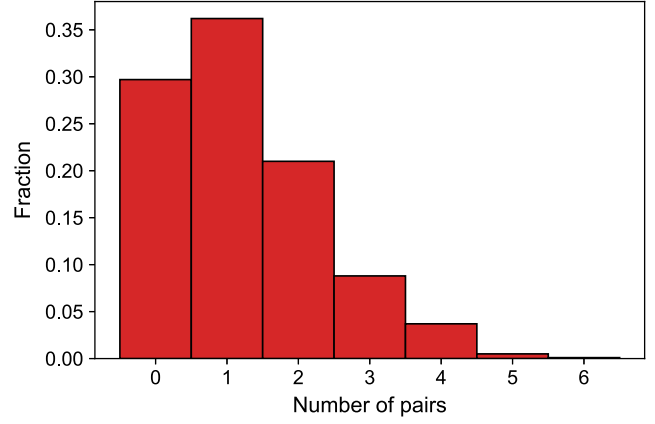


FIG. 10. Expected number of nearest-neighbor pairs per NV. The expected number of pairs with $50 < Z < 500$ Hz for a volume of $15 \times 15 \times 15$ unit cells surrounding an NV center. We estimate that pairs with a Z within the indicated region to be controllable with high fidelity. When Z is larger, it becomes comparable to X , and the control methods presented in this paper do not hold anymore. When Z is much smaller, more pulses are required in the dynamical decoupling sequence, resulting in more electron dephasing, and resolving the pair from the background bath of pairs becomes more challenging.

small Z is expected to be challenging. For every generated bath, we determine how many pairs satisfy this condition and plot the result in Fig. 10. The expected number of such nearest-neighbor pairs per NV is 1 ± 1 . Moreover, more than 70% of simulated NVs host at least one nearest-neighbor pair, indicating that such pairs can commonly be found.

In the above, we consider only nearest-neighbor pairs along the magnetic-field axis. Other pairs with smaller X and larger Z can also be detected and controlled (pair C ; see Appendix D). In Table I, we show the ten largest values of

TABLE I. The occurrence of a given coupling X when fixing one of the ^{13}C spins of the pair and moving the other around the lattice. The vector between the two ^{13}C spins of the pair is given for each X coupling in units of $a_0/4$, where a_0 is the lattice constant of diamond. All permutations of the entries of \mathbf{r} give the same coupling X .

X (Hz)	Occurrence	\mathbf{r} (in units $a_0/4$)
2062	1	[1, 1, 1]
687	3	[-1, 1, -1]
237	12	[±2, ±2, 0] and [∓2, ±2, 0]
187	3	[-1, -1, -3]
134	3	[1, 1, -3]
102	3	[1, 3, 3]
76.38	1	[-3, -3, -3]
75.95	6	[±4, ±2, ±2]
61	6	[-3, -1, 3]
46	6	[∓4, ±2, ±2]

X with their corresponding occurrence and vector \mathbf{r} between the two ^{13}C spins.

-
- [1] K. C. Miao, J. P. Blanton, C. P. Anderson, A. Bourassa, A. L. Crook, G. Wolfowicz, H. Abe, T. Ohshima, and D. D. Awschalom, *Universal Coherence Protection in a Solid-State Spin Qubit*, *Science* **369**, 1493 (2020).
- [2] N. Bar-Gill, L. M. Pham, A. Jarmola, D. Budker, and R. L. Walsworth, *Solid-State Electronic Spin Coherence Time Approaching One Second*, *Nat. Commun.* **4**, 1743 (2013).
- [3] J. T. Muhonen, J. P. Dehollain, A. Laucht, F. E. Hudson, R. Kalra, T. Sekiguchi, K. M. Itoh, D. N. Jamieson, J. C. McCallum, A. S. Dzurak, and A. Morello, *Storing Quantum Information for 30 Seconds in a Nanoelectronic Device*, *Nat. Nanotechnol.* **9**, 986 (2014).
- [4] C. E. Bradley, J. Randall, M. H. Abobeih, R. C. Berrevoets, M. J. Degen, M. A. Bakker, M. Markham, D. J. Twitchen, and T. H. Taminiau, *A Ten-Qubit Solid-State Spin Register with Quantum Memory up to One Minute*, *Phys. Rev. X* **9**, 031045 (2019).
- [5] M. D. Shulman, O. E. Dial, S. P. Harvey, H. Bluhm, V. Umansky, and A. Yacoby, *Demonstration of Entanglement of Electrostatically Coupled Singlet-Triplet Qubits*, *Science* **336**, 202 (2012).
- [6] M. D. Shulman, S. P. Harvey, J. M. Nichol, S. D. Bartlett, A. C. Doherty, V. Umansky, and A. Yacoby, *Suppressing Qubit Dephasing Using Real-Time Hamiltonian Estimation*, *Nat. Commun.* **5**, 5156 (2014).
- [7] G. Wolfowicz, A. M. Tyryshkin, R. E. George, H. Riemann, N. V. Abrosimov, P. Becker, H. J. Pohl, M. L. Thewalt, S. A. Lyon, and J. J. Morton, *Atomic Clock Transitions in Silicon-Based Spin Qubits*, *Nat. Nanotechnol.* **8**, 561 (2013).
- [8] K. Saeedi, S. Simmons, J. Z. Salvail, P. Dluhy, H. Riemann, N. V. Abrosimov, P. Becker, H. J. Pohl, J. J. Morton, and M. L. Thewalt, *Room-Temperature Quantum Bit Storage Exceeding 39 Minutes Using Ionized Donors in Silicon-28*, *Science* **342**, 830 (2013).
- [9] M. Zhong, M. P. Hedges, R. L. Ahlefeldt, J. G. Bartholomew, S. E. Beavan, S. M. Wittig, J. J. Longdell, and M. J. Sellars, *Optically Addressable Nuclear Spins in a Solid with a Six-Hour Coherence Time*, *Nature (London)* **517**, 177 (2015).
- [10] Y. Bae, K. Yang, P. Willke, T. Choi, A. J. Heinrich, and C. P. Lutz, *Enhanced Quantum Coherence in Exchange Coupled Spins via Singlet-Triplet Transitions*, *Sci. Adv.* **4**, 1 (2018).
- [11] M. H. Abobeih, J. Cramer, M. A. Bakker, N. Kalb, M. Markham, D. J. Twitchen, and T. H. Taminiau, *One-Second Coherence for a Single Electron Spin Coupled to a Multi-qubit Nuclear-Spin Environment*, *Nat. Commun.* **9**, 2552 (2018).
- [12] M. H. Abobeih, J. Randall, C. E. Bradley, H. P. Bartling, M. A. Bakker, M. J. Degen, M. Markham, D. J. Twitchen, and T. H. Taminiau, *Atomic-Scale Imaging of a 27-Nuclear-Spin Cluster Using a Quantum Sensor*, *Nature (London)* **576**, 411 (2019).
- [13] N. Zhao, J. L. Hu, S. W. Ho, J. T. Wan, and R. B. Liu, *Atomic-Scale Magnetometry of Distant Nuclear Spin Clusters via Nitrogen-Vacancy Spin in Diamond*, *Nat. Nanotechnol.* **6**, 242 (2011).
- [14] F. Shi, X. Kong, P. Wang, F. Kong, N. Zhao, R. B. Liu, and J. Du, *Sensing and Atomic-Scale Structure Analysis of Single Nuclear-Spin Clusters in Diamond*, *Nat. Phys.* **10**, 21 (2014).
- [15] C. L. Degen, F. Reinhard, and P. Cappellaro, *Quantum Sensing*, *Rev. Mod. Phys.* **89**, 035002 (2017).
- [16] J. Cramer, N. Kalb, M. A. Rol, B. Hensen, M. S. Blok, M. Markham, D. J. Twitchen, R. Hanson, and T. H. Taminiau, *Repeated Quantum Error Correction on a Continuously Encoded Qubit by Real-Time Feedback*, *Nat. Commun.* **7**, 11526 (2016).
- [17] G. Waldherr, Y. Wang, S. Zaiser, M. Jamali, T. Schulte-Herbrüggen, H. Abe, T. Ohshima, J. Isoya, J. F. Du, P. Neumann, and J. Wrachtrup, *Quantum Error Correction in a Solid-State Hybrid Spin Register*, *Nature (London)* **506**, 204 (2014).
- [18] B. Hensen, H. Bernien, A. E. Dreaú, A. Reiserer, N. Kalb, M. S. Blok, J. Ruitenbergh, R. F. Vermeulen, R. N. Schouten, C. Abellán *et al.*, *Loophole-Free Bell Inequality Violation Using Electron Spins Separated by 1.3 Kilometres*, *Nature (London)* **526**, 682 (2015).
- [19] A. Reiserer, N. Kalb, M. S. Blok, K. J. M. van Bemmelen, T. H. Taminiau, R. Hanson, D. J. Twitchen, and M. Markham, *Robust Quantum-Network Memory Using Decoherence-Protected Subspaces of Nuclear Spins*, *Phys. Rev. X* **6**, 021040 (2016).
- [20] M. Pompili, S. L. N. Hermans, S. Baier, H. K. C. Beukers, P. C. Humphreys, R. N. Schouten, R. F. L. Vermeulen, M. J. Tiggelman, L. Dos, S. Martins, B. Dirkse, S. Wehner, and R. Hanson, *Realization of a Multinode Quantum Network of Remote Solid-State Qubits*, *Science* **372**, 259 (2021).
- [21] H. Seo, A. L. Falk, P. V. Klimov, K. C. Miao, G. Galli, and D. D. Awschalom, *Quantum Decoherence Dynamics of Divacancy Spins in Silicon Carbide*, *Nat. Commun.* **7**, 12935 (2016).
- [22] M. Ye, H. Seo, and G. Galli, *Spin Coherence in Two-Dimensional Materials*, *npj Comput. Mater.* **5**, 44 (2019).
- [23] G. Q. Liu, J. Xing, W. L. Ma, P. Wang, C. H. Li, H. C. Po, Y. R. Zhang, H. Fan, R. B. Liu, and X. Y. Pan, *Single-Shot Readout of a Nuclear Spin Weakly Coupled to a Nitrogen-Vacancy Center at Room Temperature*, *Phys. Rev. Lett.* **118**, 150504 (2017).
- [24] N. Kalb, J. Cramer, D. J. Twitchen, M. Markham, R. Hanson, and T. H. Taminiau, *Experimental Creation of Quantum Zeno Subspaces by Repeated Multi-spin Projections in Diamond*, *Nat. Commun.* **7**, 13111 (2016).
- [25] K. Cujia, J. Boss, K. Herb, J. Zopes, and C. Degen, *Tracking the Precession of Single Nuclear Spins by Weak Measurements*, *Nature (London)* **571**, 230 (2019).
- [26] M. Pfender, P. Wang, H. Sumiya, S. Onoda, W. Yang, D. B. R. Dasari, P. Neumann, X.-Y. Pan, J. Isoya, R.-B. Liu *et al.*, *High-Resolution Spectroscopy of Single Nuclear Spins via Sequential Weak Measurements*, *Nat. Commun.* **10**, 594 (2019).
- [27] S. Chen, M. Raha, C. M. Phenicie, S. Ourari, and J. D. Thompson, *Parallel Single-Shot Measurement and Coherent Control of Solid-State Spins below the Diffraction Limit*, *Science* **370**, 592 (2020).

- [28] A. Ruskuc, C.-J. Wu, J. Rochman, J. Choi, and A. Faraon, *Nuclear Spin-Wave Quantum Register for a Solid State Qubit*, arXiv:2108.12723.
- [29] T. P. Harty, D. T. C. Allcock, C. J. Ballance, L. Guidoni, H. A. Janacek, N. M. Linke, D. N. Stacey, and D. M. Lucas, *High-Fidelity Preparation, Gates, Memory, and Readout of a Trapped-Ion Quantum Bit*, *Phys. Rev. Lett.* **113**, 220501 (2014).
- [30] C. Langer, R. Ozeri, J. D. Jost, J. Chiaverini, B. DeMarco, A. Ben-Kish, R. B. Blakestad, J. Britton, D. B. Hume, W. M. Itano, D. Leibfried, R. Reichle, T. Rosenband, T. Schaetz, P. O. Schmidt, and D. J. Wineland, *Long-Lived Qubit Memory Using Atomic Ions*, *Phys. Rev. Lett.* **95**, 060502 (2005).
- [31] P. Wang, C. Y. Luan, M. Qiao, M. Um, J. Zhang, Y. Wang, X. Yuan, M. Gu, J. Zhang, and K. Kim, *Single Ion Qubit with Estimated Coherence Time Exceeding One Hour*, *Nat. Commun.* **12**, 233 (2021).
- [32] B. M. Terhal, *Quantum Error Correction for Quantum Memories*, *Rev. Mod. Phys.* **87**, 307 (2015).
- [33] Note that (near-)identical spin pairs are also explored in liquid-state ensemble NMR, for example, for long-lived singlet states and spin polarization through parahydrogen [34–36].
- [34] K. F. Sheberstov, A. S. Kiryutin, C. Bengs, J. T. Hill-Cousins, L. J. Brown, R. C. Brown, G. Pileio, M. H. Levitt, A. V. Yurkovskaya, and K. L. Ivanov, *Excitation of Singlet-Triplet Coherences in Pairs of Nearly-Equivalent Spins*, *Phys. Chem. Chem. Phys.* **21**, 6087 (2019).
- [35] J. A. Jones, *Quantum Computing with NMR*, *Prog. Nucl. Magn. Reson. Spectrosc.* **59**, 91 (2011).
- [36] *Long-Lived Nuclear Spin Order*, edited by G. Pileio (Royal Society of Chemistry, London, 2020).
- [37] N. Zhao, S. W. Ho, and R. B. Liu, *Decoherence and Dynamical Decoupling Control of Nitrogen Vacancy Center Electron Spins in Nuclear Spin Baths*, *Phys. Rev. B* **85**, 115303 (2012).
- [38] See Supplemental Material at <http://link.aps.org/supplemental/10.1103/PhysRevX.12.011048> for details on the spin-pair coherence regimes and calibration of the spin and parity measurements.
- [39] D. A. Lidar, I. L. Chuang, and K. B. Whaley, *Decoherence-Free Subspaces for Quantum Computation*, *Phys. Rev. Lett.* **81**, 2594 (1998).
- [40] P. W. Anderson and P. R. Weiss, *Exchange Narrowing in Paramagnetic Resonance*, *Rev. Mod. Phys.* **25**, 269 (1953).
- [41] V. V. Dobrovitski, A. E. Feiguin, R. Hanson, and D. D. Awschalom, *Decay of Rabi Oscillations by Dipolar-Coupled Dynamical Spin Environments*, *Phys. Rev. Lett.* **102**, 237601 (2009).
- [42] O. Gühne and G. Toth, *Entanglement Detection*, *Phys. Rep.* **474**, 1 (2009).
- [43] C. E. Bradley, S. W. de Bone, P. F. W. Moller, S. Baier, M. J. Degen, S. J. H. Loenen, H. P. Bartling, M. Markham, D. J. Twitchen, R. Hanson, D. Elkouss, and T. H. Taminiau, *Robust Quantum-Network Memory Based on Spin Qubits in Isotopically Engineered Diamond*, arXiv:2111.09772.
- [44] T. Unden, P. Balasubramanian, D. Louzon, Y. Vinkler, M. B. Plenio, M. Markham, D. Twitchen, A. Stacey, I. Lovchinsky, A. O. Sushkov, M. D. Lukin, A. Retzker, B. Naydenov, L. P. McGuinness, and F. Jelezko, *Quantum Metrology Enhanced by Repetitive Quantum Error Correction*, *Phys. Rev. Lett.* **116**, 230502 (2016).
- [45] V. Vorobyov, S. Zaiser, N. Abt, J. Meinel, D. Dasari, P. Neumann, and J. Wrachtrup, *Quantum Fourier Transform for Nanoscale Quantum Sensing*, *npj Quantum Inf.* **7**, 124 (2021).
- [46] M. Pfender, N. Aslam, H. Sumiya, S. Onoda, P. Neumann, J. Isoya, C. A. Meriles, and J. Wrachtrup, *Nonvolatile Nuclear Spin Memory Enables Sensor-Unlimited Nanoscale Spectroscopy of Small Spin Clusters*, *Nat. Commun.* **8**, 834 (2017).
- [47] Y. Matsuzaki, T. Shimo-Oka, H. Tanaka, Y. Tokura, K. Semba, and N. Mizuochi, *Hybrid Quantum Magnetic-Field Sensor with an Electron Spin and a Nuclear Spin in Diamond*, *Phys. Rev. A* **94**, 052330 (2016).
- [48] S. Zaiser, T. Rendler, I. Jakobi, T. Wolf, S. Y. Lee, S. Wagner, V. Bergholm, T. Schulte-Herbruggen, P. Neumann, and J. Wrachtrup, *Enhancing Quantum Sensing Sensitivity by a Quantum Memory*, *Nat. Commun.* **7**, 12279 (2016).
- [49] A. Ajoy, U. Bissbort, M. D. Lukin, R. L. Walsworth, and P. Cappellaro, *Atomic-Scale Nuclear Spin Imaging Using Quantum-Assisted Sensors in Diamond*, *Phys. Rev. X* **5**, 011001 (2015).
- [50] N. H. Nickerson, Y. Li, and S. C. Benjamin, *Topological Quantum Computing with a Very Noisy Network and Local Error Rates Approaching One Percent*, *Nat. Commun.* **4**, 1756 (2013).
- [51] J. F. Haase, Z. Y. Wang, J. Casanova, and M. B. Plenio, *Soft Quantum Control for Highly Selective Interactions among Joint Quantum Systems*, *Phys. Rev. Lett.* **121**, 050402 (2018).
- [52] J. Casanova, Z. Y. Wang, J. F. Haase, and M. B. Plenio, *Robust Dynamical Decoupling Sequences for Individual-Nuclear-Spin Addressing*, *Phys. Rev. A* **92**, 042304 (2015).
- [53] T. K. Unden, D. Louzon, M. Zwolak, W. H. Zurek, and F. Jelezko, *Revealing the Emergence of Classicality Using Nitrogen-Vacancy Centers*, *Phys. Rev. Lett.* **123**, 140402 (2019).
- [54] B. Tratzmiller, J. F. Haase, Z. Wang, and M. B. Plenio, *Parallel Selective Nuclear-Spin Addressing for Fast High-Fidelity Quantum Gates*, *Phys. Rev. A* **103**, 012607 (2021).
- [55] S. S. Hegde, J. Zhang, and D. Suter, *Efficient Quantum Gates for Individual Nuclear Spin Qubits by Indirect Control*, *Phys. Rev. Lett.* **124**, 220501 (2020).
- [56] N. Zhao, J. Wrachtrup, and R. B. Liu, *Dynamical Decoupling Design for Identifying Weakly Coupled Nuclear Spins in a Bath*, *Phys. Rev. A* **90**, 032319 (2014).
- [57] Z. Y. Wang, J. Casanova, and M. B. Plenio, *Delayed Entanglement Echo for Individual Control of a Large Number of Nuclear Spins*, *Nat. Commun.* **8**, 14660 (2017).
- [58] J. Casanova, Z. Y. Wang, and M. B. Plenio, *Arbitrary Nuclear-Spin Gates in Diamond Mediated by a Nitrogen-Vacancy-Center Electron Spin*, *Phys. Rev. A* **96**, 032314 (2017).
- [59] T. Gullion, D. B. Baker, and M. S. Conradi, *New, Compensated Carr-Purcell Sequences*, *J. Magn. Reson.* (1969-1992) **89**, 479 (1990).